Supplementary Material

Localized plasmonic fields of nanoantennas enhance second harmonic generation from two-dimensional molybdenum disulfide

Gregory T. Forcherio,[1,2,] Luigi Bonacina,[3] Jean-Pierre Wolf,[3] and D. Keith Roper[1,4]
[1] MicroElectronics-Photonics Program, University of Arkansas, Fayetteville, AR 72701 USA
[2] Sensors & Electron Devices Directorate, U.S. Army Research Laboratory, Adelphi, MD 20783 USA
[3] Applied Physics Departement, Université de Genève, Genève 1211, Switzerland
[4] Ralph E. Martin Department of Chemical Engineering, University of Arkansas, Fayetteville, AR 72701 USA
Address all correspondence to G. T. Forcherio at gregory.t.forcherio.ctr@mail.mil

1. Heterostructure Fabrication

1.1. Fabrication

Au@SiO_x shell@core nanoantennas were drop-cast[1] onto MoS_2 monolayers fabricated via chemical vapor deposition (CVD) onto a silicon (Si) wafer with 300 nm of thermal oxide (CVD-MOS2; 2Dsemiconductors, Scottsdale, AZ USA). The 148±8 nm diameter Au@SiO_x nanoantennas (lot MGM1774; nanoComposix, San Diego, CA USA)[2] had a 15±6 nm Au shell and poly(vinylpyrrolidone) (PVP) capping agent and were dispersed in water to a concentration of $3.6x10^9$ mL^{-1}. Three microliters of Au@SiO_x-water were drop-cast onto the MoS_2-covered Si wafer, which was preheated to 105±4 ˚C to promote rapid solvent evaporation for minimized nanoantenna aggregation. Prior to drop-casting, the MoS_2-Si wafer was pre-cleaned to improve hydrophilicity by sequential 3 min immersions into acetone, methanol, and isopropanol, followed by a water rinse and dried under nitrogen gas.

1.2. Hydrophilic Treatment of CVD MoS_2

The MoS_2-covered Si wafer was pre-cleaned prior to drop-cast deposition of the Au@SiO_x nanoantennas to improve hydrophilicity. Sequential 3 min immersions of the MoS_2-coverered Si wafer in acetone, methanol, and isopropanol, followed by a water rinse and N_2 drying step, decreased water contact angle from approximately 51º to 28º, as shown in Figure S1. MoS_2 is a noted catalyst for methanol dissociation via O-H scission at sulfur vacancies in the basal plane. After the methanol immersion step in this work, removal of some MoS_2 monolayers from the Si was apparent. This was indicated by visual observation of floating inorganic precipitates in the methanol after approximately 2 minutes. The precipitates were scooped onto a glass slide and measured spectroscopically, yielding spectra that resembled spectra of MoS_2 (data not shown). However, skipping the methanol immersion step expanded the water contact angle to nearly that of the un-treated MoS_2-covered Si wafer. Thus, methanol immersion in between acetone and isopropanol was deemed necessary to achieving a wettable substrate for minimal nanoantenna aggregation upon drop-casting.

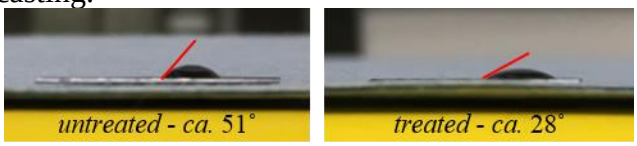

FIG. S1. Water contact angle for a MoS_2-covered Si wafer (LHS) untreated and (RHS) treated with sequential immersion into acetone, methanol, and isopropanol.

Nitric acid treatment, an alternative hydrophilic treatment commonly used on borosilicate glass, appeared to structurally degrade the MoS_2. Figure S2 shows SEM of a two different MoS_2 samples from the same CVD growth, (a) without and (b) with exposure to dilute nitric acid (37% by volume). The MoS_2 monolayers treated with nitric acid appeared jagged with anisotropic contrast in the SEM. Chemical handbooks indicate MoS_2 is impervious to nitric acid. However, such data could be unreliable in the monolayer limit. Data comprising chemical handbooks was likely based upon mass balances applied to bulk MoS_2 immersed into nitric acid solutions.

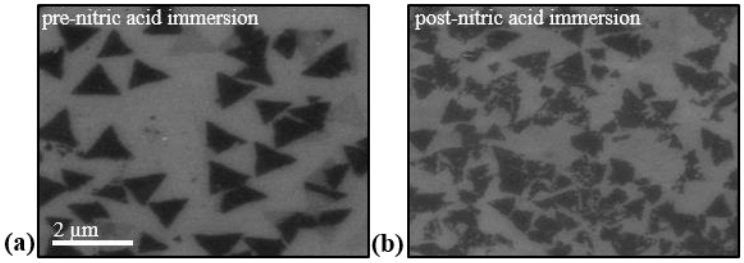

FIG. S2. Representative MoS_2 monolayers (a) before and (b) after exposure to a 37% nitric acid solution. These images were taken from a different sample than that presented in the manuscript subjected to SHG experimentation.

1.3. Optimization of Nanoantenna Drop-Cast Conditions

A series of experiments studying drop-cast outcomes of the $Au@SiO_x$ nanoantennas at various droplet volumes onto nitric-acid treated SiO_2 glass slides were conducted. Briefly, 3, 4, and 5 µL droplets of the aqueously dispersed $Au@SiO_x$ nanoantennas were pipetted onto to a 105±4 ºC pre-heated glass slide while controlling (i) ambient conditions (24 ºC, convective flow, etc.), (ii) nanoantenna-water solution temperature (13 minutes post-removal from refrigerator), (iii) and glass pre-heat warm up time (3 minutes). The resultant droplet diameter after drying, water evaporation time, and nanoantenna deposition number density were measured. Figure S3 schematically depicts a typical deposition pattern after evaporation of the water droplet, leaving behind nanoantennas dispersed onto a substrate. Total diameter of the droplet was 3.5±0.5 mm, 4.5±0.25 mm, and 7.5±0.5 mm for the 3, 4, and 5 µL volumes, respectively. Evaporation time after droplet deposition was 2.5-3.5 s, 3-5 s, and 5-6 s, respectively. Aggregation of nanoantennas was assumed to increase with evaporation time. Optical 100x bright-field reflection imaging of area (i) and (ii) for the 3 µL droplet revealed that approximate inter-nanoantenna spacing in each area was 700-900 nm and 400 nm, respectively. By comparison, the size of each CVD MoS_2 monolayer domain was approximately 1 µm in length (~$4x10^5$ nm^2 area). Thus, the 3 µL volume was chosen for the "final" deposition onto a pre-characterized CVD MoS_2 sample to provide nearly 1 nanoantenna per MoS_2 monolayer. Changing the various temperature conditions and/or nanoantenna concentration in solution would have changed these outcomes.

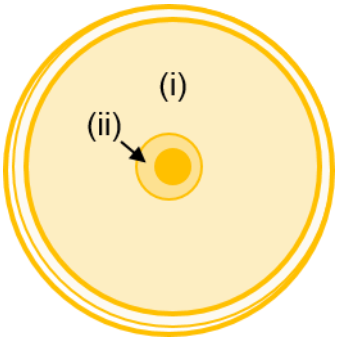

FIG. S3. Typical drying pattern of a nanoantenna-water solution drop cast onto a preheated glass substrate above the water boiling point. Lines represent contact line pinning events. Density of deposited nanoantennas within the cartoon schematic scales with opacity. Areas labeled (i) and (ii) exhibit uniformly dispersed, un-aggregated nanoantennas. Center is a visible, opaque agglomerate of nanoantennas.

2. Characterization Methodology Details

2.1. Electron Microscopy

Scanning electron microscopy (SEM) was performed on a field-emission Philips XL40 (FEI, Hillsboro, OR USA) operated at 5 kV accelerating voltage. Accelerating voltages higher than 5 kV lowered the contrast between the MoS_2 and underlying Si wafer due to higher electron penetration into the Si, resulting in more background secondary electrons. Accelerating voltages lower than 5 kV rendered the MoS_2 nearly unobservable in the presence of the metallic NA, due to their high electron scattering cross section.

Scanning transmission electron microscopy (STEM) of Au@SiO_x nanoantennas in absence of MoS_2 was performed on a FEI Tecnai F-20 (FEI, Hillsboro, OR USA) operated at 120 kV. Approximately 5 µL of the aqueously dispersed Au@SiO_x nanoantennas was drop-cast onto 20 nm thick SiO_2 membranes (SPI Supplies, West Chester, PA USA) preheated to 105±4 ºC. 5 µL of volume was chosen for TEM to increase sample size, as opposed to the 3 µL used for deposition onto CVD MoS_2 for optimal inter-nanoantenna spacing. PVP surfactant was removed to minimize carbon build-up during STEM imaging by 15 s exposure to O_2 plasma.

2.2 Nonlinear Multiphoton Microscopy

SHG from monolayer MoS_2 in the presence and absence of Au@SiO_x nanoantennas was measured with an inverted, laser-scanning multiphoton microscope (A1R-MP; Nikon Instruments Europe, Amsterdam, NLD) coupled to a wavelength tunable Ti:Sapphire laser (MaiTai Deep See; Spectra-Physics, Santa Clara, CA USA). A 60x water-immersion objective (1.27 NA CFI Plan Apo IR; Nikon Instruments) focused the rastering laser (100 fs pulse width; 80 MHz) onto the sample. Scattered photons were episcopically collected and delivered to an array of 32 photomultiplier tubes (PMT) at 2.5 nm wavelength binning. Excitation wavelengths were 810-1000 nm in 10 nm steps. Data were captured at 1.1 µs dwell time per pixel, gained by the PMT at 160 V, and averaged over 16 acquisitions to improve signal-to-noise ratio. Peak intensity of the laser was approximately 100 GW cm^{-2} across all excitation wavelengths. Diameter of the focused laser beam was 1 µm, estimated by the Abbe criterion [3]. Post-processing of hyperspectral images, including extraction of emission spectra from equi-area regions of interest (ROI) encompassing MoS_2 and/or Au@SiO_x nanoantenna(s), was performed in Nikon NIS-Elements Confocal v4.3.

2.3. Quantitation of SHG from Nonlinear Microscopy

Area normalized SHG intensity was extracted from a ROI encompassing a single Au@SiO_x nanoantenna-MoS_2 heterostructure, an isolated MoS_2 monolayer, or an isolated Au@SiO_x nanoantenna. ROI for each MoS_2 site (with or without Au@SiO_x nanoantennas) was selected based on its triangular boundaries, which were identified post-acquisition by maximizing image brightness/contrast settings in Nikon NIS-Elements Confocal v4. ROI for each isolated Au@SiO_x nanoantenna was a circle with equivalent pixel area as the triangular ROI for MoS_2 sites. Total SH intensity at a given excitation wavelength was taken as raw spectral intensity (normalized to the ROI area automatically by the software) integrated across the finite SH full width at half maximum (FWHM). The FWHM of detected SHG ranged from 3.4 nm to 4.0 nm, depending on the excitation wavelength.

Each examined nanoantenna-MoS_2 heterostructure, nanoantenna, or MoS_2 monolayer domain is labeled in Figure S4, along with the particular structures from which data are presented in Figures 2-5 of the manuscript. Two MoS_2 controls were used in calculation of the SHG enhancement factor, X, for each of the heterostructures, with specific crystals chosen according to

(i) their proximity/distance to the heterostructure in the *y* direction (i.e., vertical), (ii) size relative to the MoS_2 component of the heterostructure, and (iii) imaged SHG resembling the triangular area imaged in SEM. Criteria (i) was chosen because of focal point fluctuations along the *y* axis due to imperfect sample mounting in the microscope and differences in adsorbed chemical residuals between contact line pinning events (labeled) during the drop-cast procedure. No SHG intensity fluctuations arising from focal point drift were observed along the *x* direction. Both of these influences were anticipated to effect ultimate intensity of SHG.

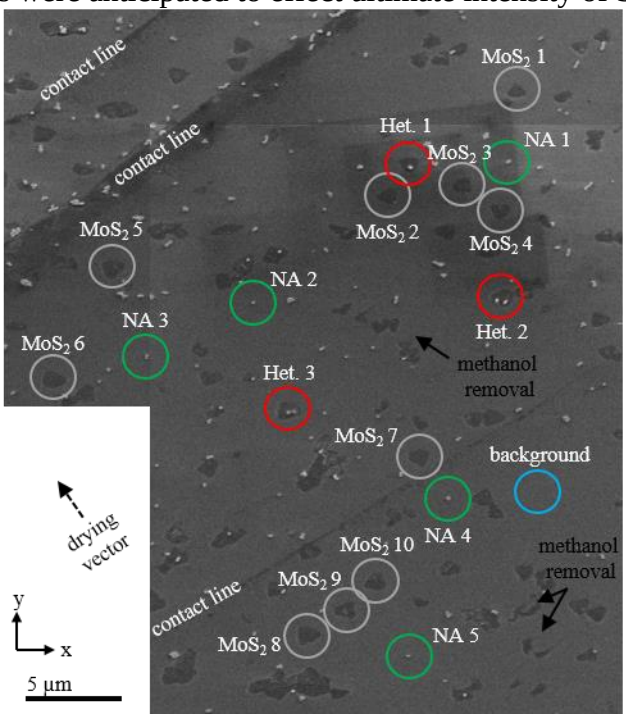

Figure 2
(red) - Het. 1
(gray) - MoS_2 3

Figure 3
(a) - mean(all MoS_2)
(b) - mean(all NA)

Figure 4
(blue) - (Het. 2)/mean(MoS_2 4 and 5)
(black) - (Het. 3)/mean(MoS_2 6 and 7)

Figure 5
(red *X*) - (Het. 1)/mean(MoS_2 2 and 3)
(blue *X*) - (Het. 2)/mean(MoS_2 4 and 5)
(black *X*) - (Het. 3)/mean(MoS_2 6 and 7)

background subtracted from all

FIG. S4. SEM of area studied by multiphoton microscopy with nanoantenna-MoS_2 heterostructures and the MoS_2 and nanoantenna controls identified/labeled. Image was assembled from two overlapping SEM micrographs. Structures from which data are presented in Figures 2-5 in the manuscript are labeled. Note that the circles do not reflect their actual ROI within Nikon NIS-Elements software, from which SHG information was extracted. Appearance of MoS_2 effected by the methanol exposure during pre-cleaning are identified.

Despite lack of SHG response, single nanoantennas were identified in the multiphoton images by using a secondary image acquisition methodology based on a 2D transformation of z-scanned volumetric maximum 2ω images. Figure S5(a) shows scattered 400-480 nm light detected over a 5 µm z-scan, i.e., ±2.5 µm around the MoS_2-substrate interface, from a 820 nm excitation beam. Figure S5(b) translates 5(a) into a 2D projection of the maximal detected intensity at each wavelength spanning 400-480 nm. The MoS_2 only emitted SHG (c) while the nanoantennas broadband luminesced (d). Excluding the dominant SHG wavelength channels (i.e., peak of the Gaussian-shaped SHG profile) allowed superposition of the two material contributions to be viewed together in (e), which matched the SEM of Figure S4. Examination of (d) or (e) allowed singular nanoantennas to be identified in corroboration with SEM images. These allowed heterostructure morphology to be characterized via independent correlative SEM to attribute their underlying physical/optical features to measured SHG activity in the multiphoton microscope.

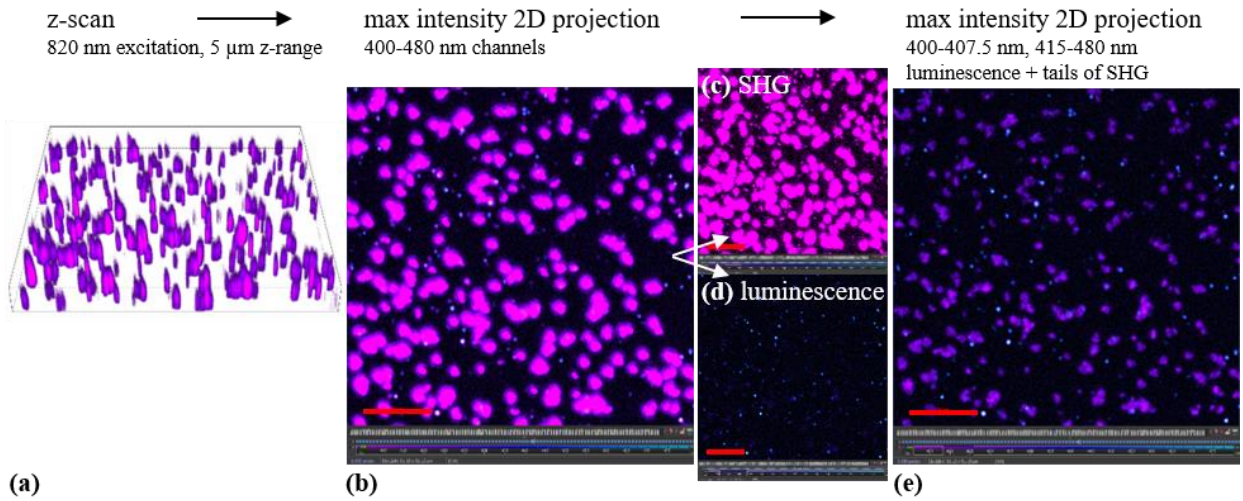

FIG. S5. Imaging methodology to distinguish single NA which did not emit SHG in the multiphoton microscope and compare with SEM to attribute structure morphology underlying measured SHG. (a) Scattered 2ω/SHG photons from 820 nm excitation detected at ±2.5 μm around the focal point (i.e., 5 μm total z-scan). (b) 2D translation of the maximum intensity detected at each pixel in (a). (c)/(d) Spectral micrographs of the SHG/luminescence components of (b). (e) Combination of (c) and (d) sans the dominant SHG wavelengths to allow facile identification of Au@SiO_x nanoantennas via their broad 2ω luminescence and MoS_2 via tails of their Gaussian SHG. Scale bars are 10 μm.

3. Numerical Computation Methods

3.1. Discrete Dipole Computation

Far-field linear optical extinction, local electric near-field enhancement ($\gamma = \boldsymbol{E}/\boldsymbol{E}_o$), and polarizability[4] of the Au@SiO_x nanoantenna in the presence/absence of a MoS_2 monolayer-covered oxide was simulated by the discrete dipole approximation (DDA) package DDSCAT (v7.3)[5–7] following established procedures.[8] Briefly, the heterostructures were translated to three-dimensional ensembles of dipoles susceptible to linear polarization from an electromagnetic plane wave according to their linear dielectric permittivity, $\chi_\omega^{(1)}$. Dielectric functions for Au, SiO_x, and monolayer MoS_2 were taken from Johnson and Christy,[9] Malitson,[10] and Mukherjee[11] *et al.*

3.2. Target Generation

Targets for the DDA were constructed with a freely available nanoHUB tool.[12] The Au@SiO_x nanoantennas were modeled as a 120 nm SiO_x core encapsulated by a homogenous 15 nm thick Au shell. Thermal oxide of the Si wafer was used as the substrate. The unoxidized Si was neglected because its 300 nm separation from the Au@SiO_x nanoantenna precluded a significant screening interaction with the surface plasmon resonance.[13] Cylindrical geometry of the substrate was based on established protocols.[14] For simulations including the MoS_2 monolayer, the top plane of substrate dipoles in contact with the nanoantenna were re-classified as monolayer MoS_2 instead of thermal oxide. Figure S6 shows a cross-section of the Au@SiO_x nanoantenna-MoS_2 heterostructure upon SiO_x, with the wavevector and polarization labeled. Au, SiO_x, and MoS_2 are shown as yellow, light blue, and green, respectively. Simulation of optical extinction spectra used a 3 nm inter-dipole spacing to balance computation time with sufficient dipoles comprising the Au shell to allow numerical convergence. Extinction spectra for nanoantenna dimers at 280 nm and 170 nm gaps were calculated assuming an infinite chain of nanoantennas at the appropriate spacing (i.e., 430 nm and 320 nm, respectively) by integrating inter-particle interactions into the Mueller scattering matrix.[6] This approach significantly eased computational requirements and time over manual construction and simulation of a nanoantenna dimer target, which the authors acknowledge would have been more rigorous. Enhanced electric near-field simulations used 1 nm inter-dipole spacing. Simulations were all performed on 16-core processor nodes with 32 GB of memory.

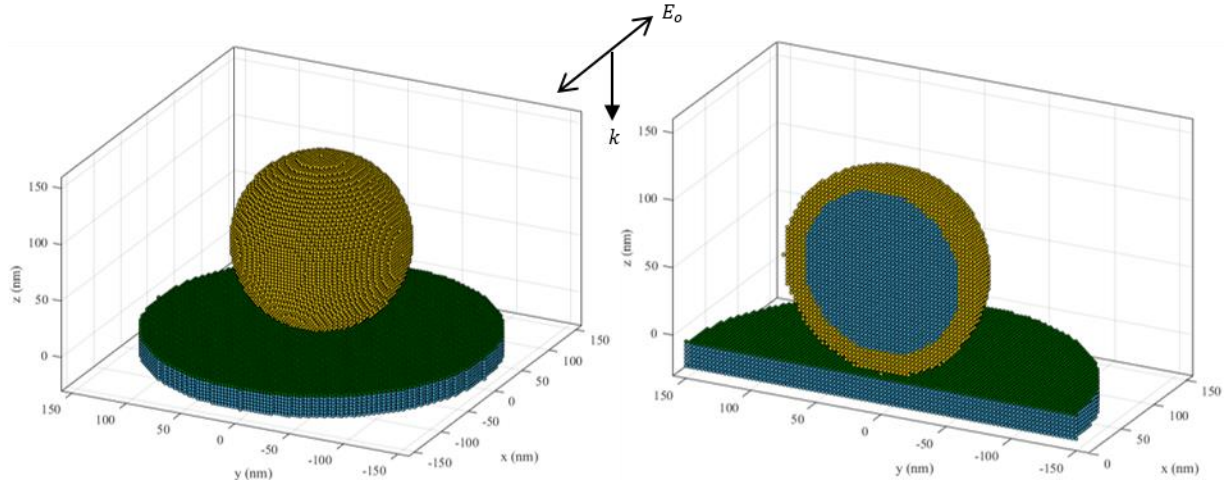

FIG. S6. DDA target of the Au@SiO_x nanoantenna-MoS_2 heterostructure atop thermal oxide of a Si wafer. RHS is a cross section to show the SiO_x core of the nanoantenna. Total dipole count was 120,182 with a 3 nm inter-dipole spacing.

3.3. Extending DDSCAT into Nonlinear Optical Regime via Miller's Rule

A nonlinear extension of the DDA was implemented via Miller's rule to estimate the monolayer MoS_2 bulk-like $\chi^{(2)}$. Miller's rule states that the ratio between nonlinear $\chi^{(2)}$ to the product of linear susceptibilities, $\chi^{(1)}$, at the input and output frequencies is nearly constant for all non-centrosymmetric condensed matter.[15,16] In other words, the nonlinear response is directly related to the linear response scaled by a proportionality factor, which is comprised of material constants. The DDSCAT readily calculates linear polarizability to the Lattice Dispersion Relation,[4] which may be converted to $\chi^{(1)}$. Thereby DDA offered an accessible, *a priori* method to evaluate second-order nonlinear optical behavior of monolayer MoS_2 at significantly less computational cost than density functional theory (DFT), density matrix theory (DMT), or the Bethe-Salpeter exciton (BSE) method provided the (i) availability of an accurate dielectric function and (ii) lack of crystalline inversion symmetry. Miller's rule was not applied to heterostructures of MoS_2 and $Au@SiO_x$ nanoantennas because (i) DDA formalism cannot limit calculation of the linear polarizability (i.e., related to $\chi^{(1)}$) to a substituent of a nanoantenna-TMD heterostructure/target and (ii) Miller's rule is ill-suited to describe SHG involving plasmonic interactions, as detailed recently by Butet and Martin.[17]

A 2D rectangular sheet of MoS_2 was discretized into point dipoles with a material-characteristic dielectric response of CVD MoS_2 measured by Mukherjee *et al.*[11] DDSCAT calculated its complex linear polarizability[18] absent any nanoantenna using a custom code implementation described previously.[4,19,20] Translation to $\chi^{(2)}$ assumed the imaginary component of polarizability, due to its direct impact on light radiation/scattering.[21] The Miller proportionality factor is a function of material constants: free space permittivity ϵ_o, electron mass e, carrier density $N \sim 10^{22}$ cm^{-3}, electron charge e, and some nonlinear strength coefficient a. Equation (S1) expresses Miller's rule in the context of SHG.[16]

$$\chi_{2\omega}^{(2)} = \frac{{\epsilon_o}^2 ma}{N^2 e^3} \chi_{2\omega}^{(1)} \left[\chi_{\omega}^{(1)}\right]^2 \quad \text{(S1)}$$

Displacement of charge from equilibrium in a nonlinear Lorentz oscillator can be estimated to be on the order of inter-atomic separation, d, such that $a \sim {\omega_o}^2/d$, where ω_o is some resonant oscillation frequency.[16] The C exciton transition for MoS_2 was assumed for ω_o herein (closest resonance state within the 2ω wavelengths) and 2.7 Å for d (the {100} planes).[22]

The bulk-like $\chi^{(2)}$ calculated with this approach is shown in Figure S7, along with other results in the literature. A 1642 pm V^{-1} maxima at 444 nm occurred for MoS_2, due to two-photon interaction with the C exciton resonance. Theoretical estimates by density functional theory (DFT), density matrix theory (DMT), and the Bethe-Salpeter exciton method (BSE) have also found $\chi^{(2)}$ dependence on the C exciton in this spectral region,[23–25] consistent with these data and those reported experimentally by Malard *et al.*[26] Response in the single-photon spectrum (i.e., above 700 nm) is relatively constant and thus had little impact to $\chi^{(2)}$ despite quadratic dependence in Equation (S1). Although the absolute magnitude of calculated $\chi^{(2)}$ could be reflective of the chosen simulation conditions, its frequency-dependent profile was identical to the measurements herein [see Figure 3(a)] and a variety of more computationally intensive calculations with reasonable magnitude agreement.

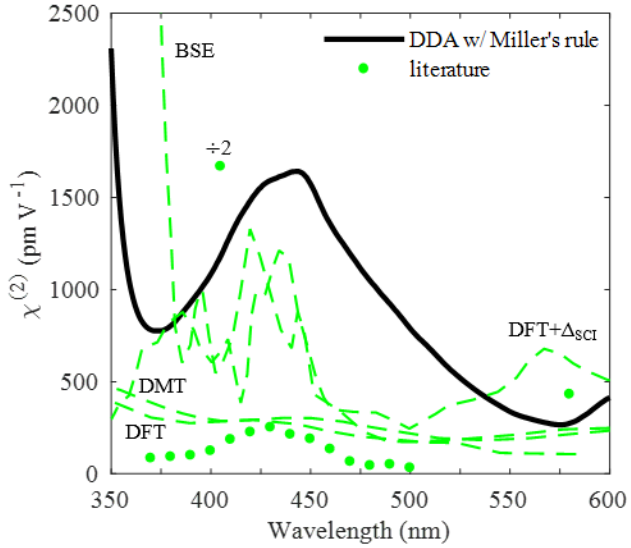

FIG. S7. Bulk-like $\chi_{\omega}^{(2)}$ for MoS_2 calculated by Miller's rule adapted to the linear DDA. Literature measurements (circles) and theoretical models (dashed lines) by DFT (with and without scissors correction, Δ_{SCI}), DMT, and BSE from Refs. 23–25 are superposed for comparison.

4. Raman Spectroscopy of CVD MoS_2

Figure S8 shows Raman spectra of the CVD-grown MoS_2,[27] whose E_{2g}^1 and A_{1g} frequencies confirmed monolayer thickness. The E_{2g}^1 peak corresponds to in-plane vibrations of chalcogens against the transition metal, which are dominated by inter-layer Coulombic screening interactions.[28,29] The A_{1g} peak corresponds to out-of-plane opposing vibrations of chalcogens, which are dominated by van der Waals forces between layers.[28] The E_{2g}^1 and A_{1g} Raman peaks were observed at 385 cm^{-1} and 407 cm^{-1}, respectively. These frequencies fell within reported thresholds for monolayers.[28] Intensity and width of Raman signatures vary arbitrarily between samples and hold no information.[28]

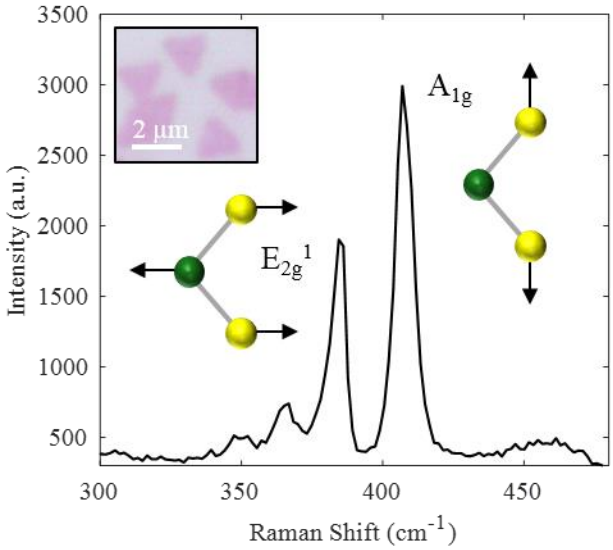

FIG. S8. Raman spectra of CVD-synthesized MoS_2 on SiO_x. In-plane E_{2g}^1 and out-of-plane A_{1g} vibrational modes are labeled and shown schematically. Optical image from measured area is inset. Excitation wavelength was 488 nm.

5. Raw SHG from Ten MoS_2 Monolayers

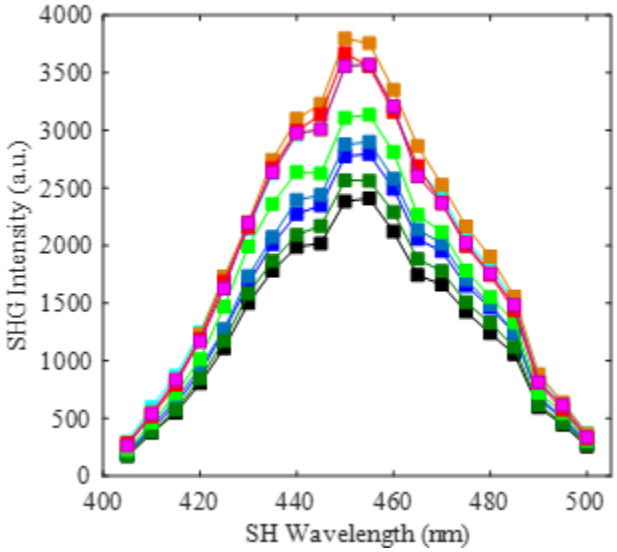

FIG. S9. Integrated SHG intensity versus central SH wavelength detected from ROI drawn around ten CVD MoS_2 monolayers, where the magnitude variation arose from minute differences in monolayer size.

6. Au@SiO_x Nanoantenna Optical Characterization and Modeling

The Au@SiO_x nanoantennas exhibited a 817 nm dipole and 625 nm quadrupole LSPR, respectively, in water. Figure S10(a) shows measured absorbance of the nanoantennas in a cuvette (solid) and theoretical optical extinction calculations by DDA and Mie theory (dashed and dotted). Screening by the PVP surfactant (RI = 1.52) was considered as a 1.40 effective refractive index environment with the water (RI = 1.33). The dipole radiation pattern is shown in the electric near-field enhancement plot (truncated at 5) of Figure S10(b); full range of the enhancement is approximately 0-8. This work focused on SHG enhancements by the resonant dipole mode. Experimental LSPR linewidth in (a) reflects the nanoantenna size distribution in solution.

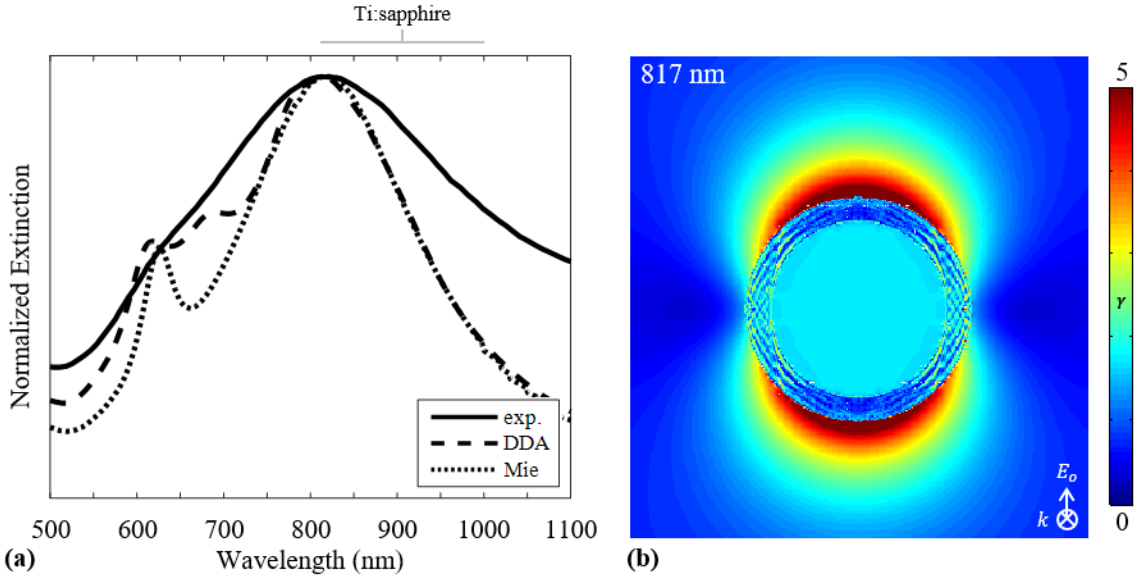

FIG. S10. (a) Normalized extinction spectra for the Au@SiO_x nanoantennas in water according to transmission UV-vis measurements (solid), DDA (dashed), and Mie theory (dotted). Results from DDA and Mie theory were taken at an effective refractive index of 1.40, 0.07 higher than pure water to account for PVP ligands on the Au. (b) Electric near-field enhancement (γ) truncated to 5 at the 817 nm dipole LSPR.

7. DDA Modeling of Au@SiO_x-MoS_2 Heterostructures

7.1. Nanoantenna Control Spectra

Figure S11 shows optical extinction spectra of water-immersed Au@SiO_x nanoantenna monomers (red line) and dimers at a 280 nm (blue line) and 170 nm (black line) gap, respectively, in the absence of MoS_2. Strength of the enhanced local electric field is proportional to magnitude of optical extinction in the spectra. Trends in these spectra correspond to the respective profiles of enhanced SHG measured from dimeric nanoantenna-MoS_2 heterostructures in Figure 4. The higher X in Figure 4 exhibited by the 170 nm gap dimer in the 800-890 nm range relative to the 280 nm gap dimer appears counter to the extinction magnitudes shown in Figure S11. This may be attributable to changes in extinction efficiency upon inclusion of the MoS_2 and the fact that the local field around nanoantennas differs from the field at its interface with a MoS_2 sublayer.

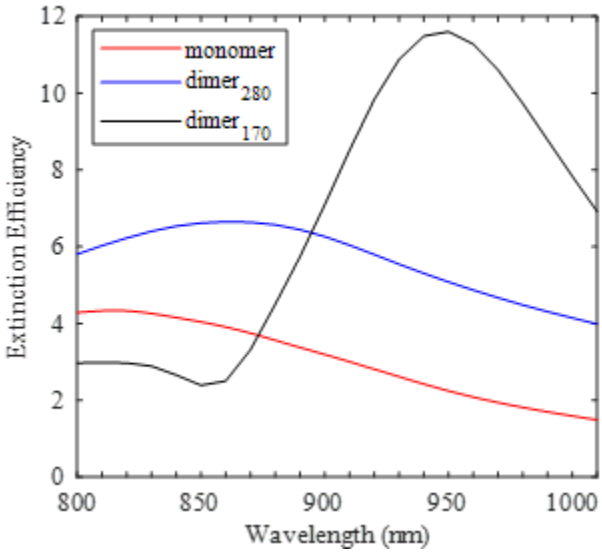

FIG. S11. Calculated extinction spectra for Au@SiO_x nanoantenna monomers (black) and dimers with a 280 nm (blue) and 170 nm (black) inter-particle gap. Extinction efficiency shown for the dimers was that from polarization parallel with the dimer axis.

7.2. Extinction Spectrum and Peak Attribution

Figure S12 shows calculated linear optical extinction efficiency spectra for a Au@SiO_x nanoantenna-MoS_2 heterostructure atop SiO_x (to account for thermal oxide on the Si wafer) sans any nonlinear optical effects. Optical intensity enhancement, γ^2, maps taken at each resonance mode are also shown: top row plots are truncated to 20 and bottom row plots are truncated to 5 for clarity. Maximas corresponding to MoS_2 C exciton, MoS_2 B exciton coupled with the Au@SiO_x quadrupole LSPR, MoS_2 A exciton, and Au@SiO_x dipole LSPR were observed at 450 nm, 623 nm, 660 nm, and 820 nm, respectively. Full range of the field intensity enhancement (γ^2) under 820 nm irradiation was 0-60 and 0-5 for the top and bottom plots, respectively. The dipole and quadrupole LSPR of the Au@SiO_x nanoantenna both red-shifted 3 nm from screening by the MoS_2 monolayer, consistent with related measurements.[8] Single photon (ω) and two-photon frequency (2ω) ranges accessible by the 810-1000 nm excitation spectrum used herein are labeled red and blue, respectively, for reference.

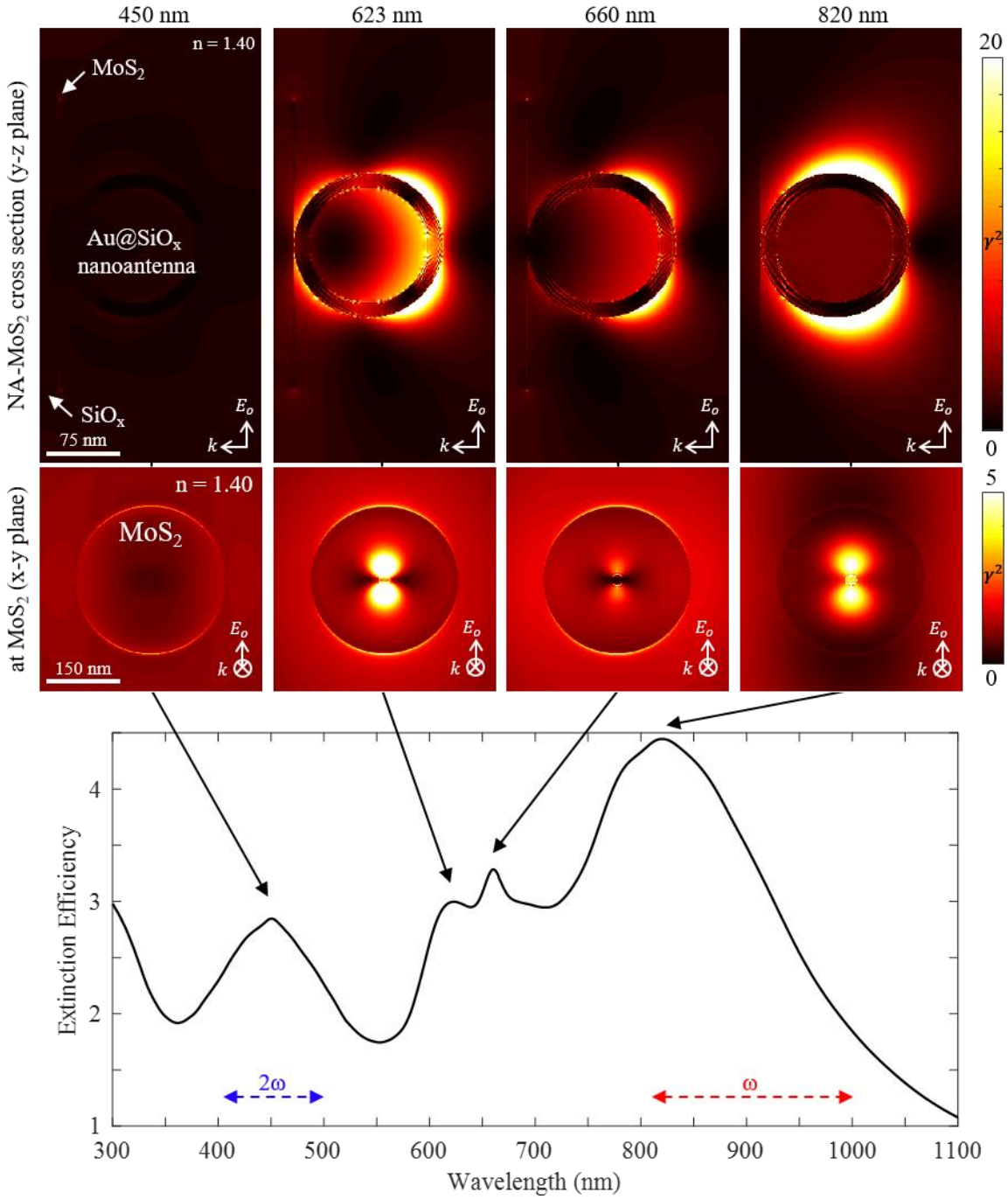

FIG. S12. Calculated linear optical extinction efficiency of a heterostructure comprised of a Au@SiO_x nanoantenna and MoS_2 monolayer in water. The ω excitation and 2ω detection frequencies measured herein are labeled for reference. Enhanced optical intensity (γ^2) plots at 450 nm, 623 nm, 660 nm, and 820 nm irradiation at two vantage points: (top) y-z plane cross-section of the Au@SiO_x nanoantenna and MoS_2 truncated to 20 and (bottom) x-y plane of field incident upon the MoS_2 monolayer truncated to 5. Note: the circular cross section observable in top (bottom) panels is the 150 nm-diameter nanoantenna (300 nm diameter MoS_2 plane underlying the nanoantenna). In the bottom panel, the nanoantenna is out-of-the-page (i.e., not observable) and the silica substrate underlying the MoS_2 is in-the-page. See the target visualization in Figure S6 for assistance with target orientation.

7.3. Enhanced Field Strength Incident Upon MoS_2

The enhanced optical excitation intensity at the MoS_2 monolayer by the nanoantenna was within ±5% across excitation spectrum, despite detuning from the dipole LSPR as the pump frequency was decreased from 810 nm to 1000 nm, as shown in Figure S13. This was attributable to the large, spherical morphology of the Au@SiO_x nanoantennas. Surface plasmon strength decays exponentially across space away from the nanoantenna surface.[30–32] Herein, 75 nm separated the MoS_2 monolayer from the dipole axis of the Au@SiO_x nanoantenna. Presence of PVP surfactant (~10 nm or less in length) likely exacerbated this issue. Unfortunately, the PVP could only be removed from nanoantennas subjected to STEM characterization in the absence of CVD MoS_2.

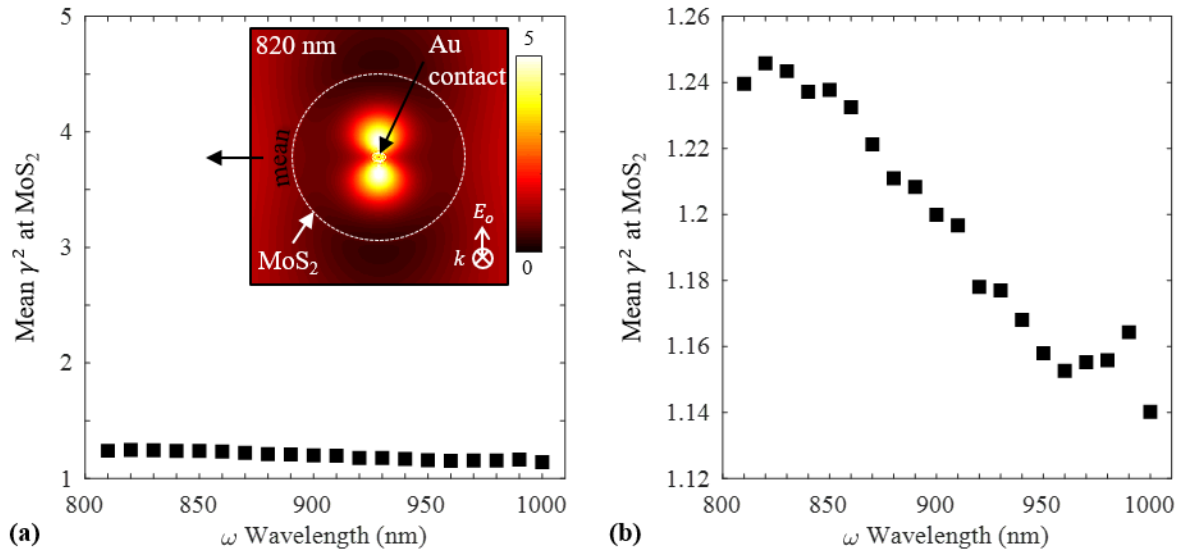

FIG. S13. Mean enhanced optical intensity incident upon a 300 nm diameter MoS_2 monolayer by a 150 nm Au@SiO_x nanoantenna calculated by DDA plotted at (a) 0 to 5 scale and (b) 1.12 to 1.26 scale. The former was chosen according to scale of corresponding enhanced optical intensity plot at 820 nm, taken verbatim from Figure S12.

In a lab frame, the enhanced field "seen" by the CVD MoS_2 was less than that simulated in Figure S13 because of the DDA-simplified representation of approximately 1 μm length triangular CVD MoS_2 as a 300 nm diameter circle, giving a 6x mismatch in MoS_2 area representation. The DDA formalism is intended for subwavelength objects as opposed to microscopic objects. Optoelectronic interaction of microscale media, such as simple dielectric (e.g., silica) and complex dielectric (e.g., indium tin oxide) substrates, with adjacent nanoantennas have been simulated by including a nm-scale portion of the media within one nanoantenna radius beyond the nanoantenna surface.[14] This simplification showed good correspondence with far-field optical measures when applied to monolayer TMD;[33] resonant optical modes were accurately depicted to within 2% of measurements. Herein, underlying silica and MoS_2 was simulated as a 150 nm radius cylinder, as the spherical nanoantenna used had a 75 nm radius (see §S3.2).

Converse to the dipole LSPR, excitation at the 623 nm quadrupole LSPR would have "delivered" more power to the MoS_2 because of closer physical proximity of its oscillating electrons to the MoS_2 monolayer. The quadrupole LSPR appears at 623 nm in Figure S12; the y-z and x-y projections of its optical intensity enhancement are shown in the upper and lower 623-nm panels, respectively. Replacement of the spherical Au@SiO_x nanoantenna with a nanoantenna offering a larger interface with the TMD, e.g., a nanorod, nanoring,[19,34,35] or nanoprism could have more effectively "delivered" optical power to the MoS_2.[8] Geometric asymmetry of nano-rods or

–prisms in the x-y plane, however, would require accounting for polarization of normally-incident irradiation, whereas spherical nanoantennas did not exhibit polarization dependence.[36] Fabrication of nanorings would generally require top-down lithography[37,38] rather than simple drop-casting.

8. Calculation of SHG Conversion Efficiency

SHG intensity, $I_{2\omega}$, radiated from a media with second-order electric susceptibility, $\chi^{(2)}$, and thickness L is governed by Equation (S2):[16,39]

$$I_{2\omega} = \frac{2\pi^2\left[\chi_{2\omega}^{(2)}\right]^2 L^2}{n_\omega^2 n_{2\omega} c\epsilon_o \lambda_\omega^2} {I_\omega}^2 \tag{S2}$$

where I_ω is the pump intensity (with frequency ω and wavelength λ), n are linear refractive indices of the media, c is the speed of light, and ϵ_o is free space permittivity. Optical intensity, I, may be expressed as $1/2\ \epsilon_o c|\boldsymbol{E}|^2$, where $|\boldsymbol{E}|$ is the electric field strength. Substitution of this relation for optical intensity into Equation (S2) yields:

$$I_{2\omega} = \frac{2\pi^2\left[\chi_{2\omega}^{(2)}\right]^2 L^2}{n_\omega^2 n_{2\omega} c\epsilon_o \lambda_\omega^2}\left[\frac{1}{2}\epsilon_o c|\boldsymbol{E}_\omega|^2\right]^2 \tag{S3}$$

Now, assuming strength of the applied pump field acting upon the nonlinearly-active material (e.g., MoS_2 in this work) is enhanced by some single-mode, local gain source (e.g., surface plasmon resonance in this work), Equation (S4) may be adjusted to include a field augmentation factor, γ:

$$\begin{aligned} I_{2\omega} &= \frac{2\pi^2\left[\chi_{2\omega}^{(2)}\right]^2 L^2}{n_\omega^2 n_{2\omega} c\epsilon_o \lambda_\omega^2}\left[\frac{1}{2}\epsilon_o c(\gamma|\boldsymbol{E}_\omega|)^2\right]^2 \\ &= \frac{2\pi^2\left[\chi_{2\omega}^{(2)}\right]^2 L^2}{n_\omega^2 n_{2\omega} c\epsilon_o \lambda_\omega^2}\gamma^4\left[\frac{1}{2}\epsilon_o c|\boldsymbol{E}_\omega|^2\right]^2 \end{aligned} \tag{S4}$$

Next, Equation (S5) re-introduces the applied I_ω definition:

$$I_{2\omega} = \frac{2\pi^2\left[\chi_{2\omega}^{(2)}\right]^2 L^2}{n_\omega^2 n_{2\omega} c\epsilon_o \lambda_\omega^2}\gamma^4 {I_\omega}^2 \tag{S5}$$

Conversion efficiency of pump energy to the SHG is defined as the ratio of $I_{2\omega}$ to I_ω, *viz.*

$$\eta_{2\omega} \equiv \frac{I_{2\omega}}{I_\omega} = \frac{\frac{2\pi^2\left[\chi_{2\omega}^{(2)}\right]^2 L^2}{n_\omega^2 n_{2\omega} c\epsilon_o \lambda_\omega^2}\gamma^4 {I_\omega}^2}{I_\omega} = \frac{2\pi^2\left[\chi_{2\omega}^{(2)}\right]^2 L^2}{n_\omega^2 n_{2\omega} c\epsilon_o \lambda_\omega^2}\gamma^4 I_\omega \tag{S6}$$

such that the SHG conversion efficiency scales with γ^4,[40] which varies with the pump frequency/wavelength for plasmonic resonances. The intrinsic SHG performance of a material independent of controllable variables (i.e., I_ω and L) has been defined as the normalized conversion efficiency, η_{norm}, with units of W^{-1}, *viz.*[41]

$$\eta'_{2\omega} \equiv \frac{I_{2\omega}}{I_\omega} = \eta_{norm} L^2 \gamma^4 I_\omega \tag{S7}$$

$$\eta_{norm} \equiv \frac{2\pi^2\left[\chi_{2\omega}^{(2)}\right]^2}{n_\omega^2 n_{2\omega} c\epsilon_o \lambda_\omega^2}\ . \tag{S8}$$

The η_{norm} for monolayer MoS_2 plotted in Figure 5 (gray line) was calculated using the Equation (S8) definition. For the nanoantenna-MoS_2 heterostructures studied in this work, γ is also an intrinsic gain source not subject to external tuning. Thus, the η_{norm} for MoS_2 in the presence of a single nanoantenna heterostructure was represented theoretically in Figure 5 (red line) by multiplying MoS_2 η_{norm} by γ^4 [equivalent to $(\boldsymbol{E}/\boldsymbol{E}_o)^2$], calculated by the DDA (see Figure S11). These γ are the local field augmentation factors "seen" by the MoS_2 induced by the plasmonic

nanoantenna after interaction with the incident field. Thus, any measured SHG enhancement factor X is equal to the γ^4 for a resonator component of the heterostructure. In the context of Figure 5, agreement between $X\eta_{norm}$ (i.e., measured) and $\gamma^4\eta_{norm}$ (i.e., theoretical) implied that observed SHG enhancements in nanoantenna-MoS_2 heterostructures were attributable to plasmonic field enhancement by the nanoantenna(s).

References

1. J. D. Torrey, T. L. Kirschling, and L. F. Greenlee: Processing and characterization of nanoparticle coatings for quartz crystal microbalance measurements. *J. Res. Natl. Inst. Stand. Technol.* **120**, 1 (2015).
2. nanoComposix lot #MGM1774.
3. H. Kuzmany: Solid-State Spectroscopy, 2nd ed. (Springer, 2010).
4. D. DeJarnette, P. Blake, G. T. Forcherio, and D. K. Roper: Far-field Fano resonance in nanoring arrays modeled from extracted, point dipole polarizability. *J. Appl. Phys.* **115**, 024306 (2014).
5. B. T. Draine and P. J. Flatau: Discrete-dipole approximation for scattering calculations. *J. Opt. Soc. Am. A* **11**(4), 1491 (1994).
6. B. T. Draine and P. J. Flatau: Discrete-dipole approximation for periodic targets: theory and tests. *J. Opt. Soc. Am. A* **25**(11), 2693 (2008).
7. P. J. Flatau and B. T. Draine: Fast near field calculations in the discrete dipole approximation for rectangular rectilinear grids. *Opt. Express* **20**(2), 1247 (2012).
8. G. T. Forcherio and D. K. Roper: Spectral characteristics of noble metal nanoparticle-molybdenum disulfide heterostructures. *Adv. Opt. Mater.* **4**(8), 1288 (2016).
9. P. B. Johnson and R. W. Christy: Optical constants of the noble metals. *Phys. Rev. B* **6**(12), 4370 (1972).
10. I. H. Malitson: Interspecimen comparison of the refractive index of fused silica. *J. Opt. Soc. Am.* **55**(10), 1205 (1965).
11. B. Mukherjee, F. Tseng, D. Gunlycke, K. Kumar, G. Eda, and E. Simsek: Complex electrical permittivity of the monolayer molybdenum disulfide (MoS2) in near UV and visible. *Opt. Mater. Express* **5**(2), 447 (2015).
12. M. Seeram, G. T. Forcherio, and D. K. Roper: *nanoHUB* (2016), DOI: 10.4231/D3J960B3D.
13. K. L. Kelly, E. Coronado, L. L. Zhao, and G. C. Schatz: The optical properties of metal nanoparticles: the influence of size, shape, and dielectric environment. *J. Phys. Chem. B* **107**(3), 668 (2003).
14. G. T. Forcherio, P. Blake, M. Seeram, D. DeJarnette, and D. K. Roper: Coupled dipole plasmonics of nanoantennas in discontinuous, complex dielectric environments. *J. Quant. Spectrosc. Radiat. Transf.* **166**, 93 (2015).
15. R. C. Miller: Optical Second Harmonic Generation in Piezoelectric Crystals. *Appl. Phys. Lett.* **5**(1), 17 (1964).
16. R. W. Boyd: Nonlinear Optics, 3rd ed. (Academic Press, 2008).
17. J. Butet and O. J. F. Martin: Evaluation of the nonlinear response of plasmonic metasurfaces: Miller's rule, nonlinear effective susceptibility method, and full-wave computation. *J. Opt. Soc. Am. B* **33**(2), A8 (2016).
18. D. Gutkowicz-Krusin and B. T. Draine: Propagation of Electromagnetic Waves on a Rectangular Lattice of Polarizable Points. *https://arxiv.org/abs/astro-ph/0403082* (2004).
19. G. T. Forcherio, P. Blake, D. DeJarnette, and D. K. Roper: Nanoring structure, spacing, and local dielectric sensitivity for plasmonic resonances in Fano resonant square lattices. *Opt. Express* **22**(15), 17791 (2014).
20. G. T. Forcherio, P. Blake, M. Seeram, D. DeJarnette, and D. K. Roper: Coupled dipole plasmonics of nanoantennas in discontinuous, complex dielectric environments. *J. Quant. Spectrosc. Radiat. Transf.* **166**, 93 (2015).

21. D. K. Roper, W. Ahn, B. Taylor, and A. G. D. Asen: Enhanced spectral sensing by electromagnetic coupling with localized surface plasmons on subwavelength structures. *IEEE Sens.* **10**(3), 531 (2010).
22. G. T. Forcherio, M. Benamara, and D. K. Roper: Electron energy loss spectroscopy of hot electron transport between gold nanoantennas and molybdenum disulfide by plasmon excitation. *Adv. Opt. Mater.* **5**(3), 1600572 (2016).
23. D. J. Clark, V. Senthilkumar, C. T. Le, D. L. Weerawarne, B. Shim, J. I. Jang, J. H. Shim, J. Cho, Y. Sim, M.-J. Seong, S. H. Rhim, A. J. Freeman, K.-H. Chung, and Y. S. Kim: Strong optical nonlinearity of CVD-grown MoS2 monolayer as probed by wavelength-dependent second-harmonic generation. *Phys. Rev. B* **90**(12), 121409 (2014).
24. S. H. Rhim, Y. S. Kim, and A. J. Freeman: Strain-induced giant second-harmonic generation in monolayered 2H-MoX2 (X = S, Se, Te). *Appl. Phys. Lett.* **107**(24), 241908 (2015).
25. M. L. Trolle, G. Seifert, and T. G. Pedersen: Theory of excitonic second-harmonic generation in monolayer MoS2. *Phys. Rev. B* **89**(23), 235410 (2014).
26. L. M. Malard, T. V. Alencar, A. P. M. Barboza, K. F. Mak, and A. M. de Paula: Observation of intense second harmonic generation from MoS2 atomic crystals. *Phys. Rev. B* **87**(20), 201401 (2013).
27. Electronic mail correspondence. 2Dsemiconductors: May 14 2015.
28. H. Li, Q. Zhang, C. C. R. Yap, B. K. Tay, T. H. T. Edwin, A. Olivier, and D. Baillargeat: From bulk to monolayer MoS2: Evolution of Raman scattering. *Adv. Funct. Mater.* **22**(7), 1385 (2012).
29. A. Molina-Sánchez and L. Wirtz: Phonons in single-layer and few-layer MoS2 and WS2. *Phys. Rev. B* **84**(15), 155413 (2011).
30. Y. Liu and X. Zhang: Metamaterials: a new frontier of science and technology. *Chem. Soc. Rev.* **40**(5), 2494 (2011).
31. S. A. Maier and H. A. Atwater: Plasmonics: localization and guiding of electromagnetic energy in metal/dielectric structures. *J. Appl. Phys.* **98**(1), 011101 (2005).
32. J. N. Anker, W. P. Hall, O. Lyandres, N. C. Shah, J. Zhao, and R. P. Van Duyne: Biosensing with plasmonic nanosensors. *Nat. Mater.* **7**(6), 442 (2008).
33. G. T. Forcherio and D. K. Roper: Spectral Characteristics of Noble Metal Nanoparticle-Molybdenum Disulfide Heterostructures. *Adv. Opt. Mater.* **4**(8), 1288 (2016).
34. J. Aizpurua, P. Hanarp, D. Sutherland, M. Käll, G. Bryant, and F. J. García de Abajo: Optical Properties of Gold Nanorings. *Phys. Rev. Lett.* **90**(5), 057401 (2003).
35. P. K. Jain, S. Eustis, and M. A. El-Sayed: Plasmon coupling in nanorod assemblies: optical absorption, discrete dipole approximation simulation, and exciton-coupling model. *J. Phys. Chem. B* **110**(37), 18243 (2006).
36. G. T. Forcherio, D. DeJarnette, M. Benamara, and D. K. Roper: Electron energy loss spectroscopy of surface plasmon resonances on aberrant gold nanostructures. *J. Phys. Chem. C* **120**(43), 24950 (2016).
37. C. Huang, J. Ye, S. Wang, T. Stakenborg, and L. Lagae: Gold nanoring as a sensitive plasmonic biosensor for on-chip DNA detection. *Appl. Phys. Lett.* **100**(17), 173114 (2012).
38. A. R. Halpern and R. M. Corn: Lithographically patterned electrodeposition of gold, silver, and nickel nanoring arrays with widely tunable near-infrared plasmonic resonances. *ACS Nano* **7**(2), 1755 (2013).
39. Y. R. Shen: The Principles of Nonlinear Optics, 1st ed. (Wiley, 1989).

40. M. Ishifuji, M. Mitsuishi, and T. Miyashita: Bottom-up design of hybrid polymer nanoassemblies elucidates plasmon-enhanced second harmonic generation from nonlinear optical dyes. *J. Am. Chem. Soc.* No. 12, 4418 (2009).
41. S. C. Kumar, G. K. Samanta, K. Devi, and M. Ebrahim-Zadeh: High-efficiency, multicrystal, single-pass, continuous-wave second harmonic generation. *Opt. Express* **19**(12), 11152 (2011).